

The nature of silicon PN junction impedance at high frequency

David A. van Nijen^{*}, Paul Procel, René A.C.M.M. van Swaaij, Miro Zeman, Olindo Isabella^{*}, Patrizio Manganiello

Delft University of Technology, Mekelweg 4, Delft, 2628 CD, The Netherlands

ARTICLE INFO

Dataset link: <https://doi.org/10.4121/19445ed8-c8d5-4204-a8c6-adaa7a55ece3>

Keywords:

Photovoltaics
Capacitance
Impedance
Admittance
PN junction
Low–high junction

ABSTRACT

A thorough understanding of the small-signal response of solar cells can reveal intrinsic device characteristics and pave the way for innovations. This study investigates the impedance of crystalline silicon PN junction devices using TCAD simulations, focusing on the impact of frequency, bias voltage, and the presence of a low–high (LH) junction. It is shown that the PN junction exhibits the behavior of a parallel resistor–capacitor circuit (RC -loop) with fixed element values at low frequencies, but undergoes relaxation in both resistance R_j and capacitance C_j as frequency increases. Moreover, it is revealed that the addition of a LH junction impacts the impedance by altering R_j , C_j , and the series resistance R_s . Finally, while various publications on solar-cell impedance model the LH junction using an RC -loop, the findings in this study indicate that such a model does not accurately represent the underlying physics. Instead, this approach is likely compensating for the frequency-dependent behavior of R_j and C_j .

1. Introduction

In photovoltaic (PV) systems, solar cells are commonly perceived as devices that produce direct current (DC) upon exposure to sunlight. Much of the research and development in solar energy focuses on enhancing the efficiency of solar cells in converting light into electrical power. However, the potential use of solar cells for high-frequency alternating current (AC) applications makes it valuable to explore and refine their impedance. For instance, studying the solar-cell impedance can rapidly gather large amounts of data for efficient and accurate measurements of a variety of solar cell parameters [1–3]. Additionally, the solar cell impedance influences the performance of power electronics that perform maximum power point tracking (MPPT) [4]. Extending this concept, it has been proposed to exploit the self-impedance of solar cells, which could lead to the development of converters that require fewer passive components at the input [5,6]. Moreover, the impedance of solar cells impacts their suitability for applications beyond energy generation, such as Visible Light Communication (VLC) systems. In such systems, where solar cells can be employed as receivers [7–9], the impedance directly influences the system's bandwidth [10,11]. These examples highlight the potential of solar-cell impedance analysis to reveal intrinsic device characteristics and pave the way for innovations.

In the context of small-signal analysis, it is well known that the PN junction impedance cannot be fully represented by any linear, lumped, finite, passive, or bilateral network [12]. Nevertheless, when the frequency is sufficiently low, the PN junction impedance can be

approximated by a parallel resistor–capacitor circuit (RC -loop), a common simplification found in literature. At these lower frequencies, the minority carrier distribution can effectively “follow” the frequency of the AC signal. Yet, as the frequency increases beyond a certain threshold, violating this condition, the RC -loop approximation loses its validity. However, it is important to mention that solar cells consist of more than just a PN junction. For example, direct metal contact to the lightly doped substrate is not appropriate, as it would lead to the formation of a Schottky barrier and/or Fermi level pinning [13]. Hence, practical devices often possess a so-called low–high (LH) junction, which reduces the contact resistance by facilitating tunneling and reduces surface recombination. However, this poses a challenge when the impedance of such a device no longer behaves like a single RC -loop beyond a certain frequency. Is this because the RC -loop approximation of the PN junction is no longer valid, or is it due to separate impedance effects in the LH junction? In publications on solar-cell impedance, an additional RC -loop is frequently incorporated into the impedance model to account for the LH junction impedance [2,4,14–17]. Moreover, sometimes a constant phase element (CPE) or a third RC -loop is introduced to solar-cell impedance models to address various non-ideal effects in devices with passivating contacts [18,19]. While these adjustments often improve fitting accuracy, the underlying physics may not be accurately captured.

In this study, the impedance of crystalline silicon (c-Si) PN junction devices is investigated through Technology Computer Aided Design

^{*} Corresponding authors.

E-mail addresses: d.a.vannijen@tudelft.nl (D.A. van Nijen), o.isabella@tudelft.nl (O. Isabella).

(TCAD) simulations. The simulated device geometry and dopant concentrations are chosen such that they resemble those of wafer-based solar cells. While this study focuses exclusively on such geometries, it is worth noting that many of results may also extend to other semiconductor PN junction devices. However, for other semiconductor materials it should be considered that there may be differences in dielectric permittivity and dominant recombination mechanisms, particularly between direct and indirect bandgap materials. The TCAD simulation methodology enables the isolation of the PN junction impedance, since ideal contacts can be positioned on a bulk material without the inclusion of a LH junction. Moreover, the almost noise-free simulation data facilitate a thorough examination of subtle shortcomings of equivalent model fits. While much of the findings in this paper also apply to c-Si solar cells with passivating contacts, this study exclusively focuses on homojunction architectures. It is crucial for the field to understand the limitations of modeling PN homojunction impedance across different frequency ranges with a resistor–capacitor circuit. Without this knowledge, non-idealities may be incorrectly attributed to other parts of the device. For instance, one outcome of this paper is that certain impedance behavior that is often attributed to capacitive effects in the LH junction, is in fact due to high-frequency effects in the PN junction. First, the paper demonstrates the frequency range within which the PN junction can be accurately represented by an RC-loop, and it explores the consequences of exceeding this frequency threshold. Subsequently, it is demonstrated how the silicon bulk properties influence these results. Finally, it is discussed how the impedance changes when a LH junction is added to the device structure.

2. Theory

In Section 2.1, the theory of PN junction admittance related to minority carrier diffusion is summarized. Subsequently, Section 2.2 outlines a more comprehensive small-signal impedance model of a PN junction, and provides equations describing the circuit element values.

2.1. PN junction small-signal admittance

When a PN junction diode is forward biased, diffusion mechanisms play an important role in the admittance. For a PN junction consisting of homogeneously doped regions, the electron diffusion current is given by [12]:

$$I_{n0} = \frac{AqD_n n_{p0}}{L_n} \exp\left(\frac{qV_F}{kT}\right) \quad (1)$$

where A is the cross-sectional area of the PN junction, q is the elementary charge constant, D_n is the diffusion constant of electrons, n_{p0} is the minority carrier electron concentration on the p side of the junction, L_n is the electron diffusion length, and V_F is the applied forward-bias voltage. Finally, k and T are the Boltzmann constant and temperature, respectively. Similarly, the hole diffusion current in a PN junction consisting of homogeneously doped regions is given by [12]:

$$I_{p0} = \frac{AqD_p p_{n0}}{L_p} \exp\left(\frac{qV_F}{kT}\right) \quad (2)$$

where D_p is the diffusion constant of holes, p_{n0} is the minority carrier hole concentration on the n side of the junction, and L_p is the hole diffusion length. Using these diffusion current expressions, the PN junction admittance can be defined as [12]:

$$Y = \frac{1}{V_t} \left[I_{p0} \sqrt{1 + i\omega\tau_{p0}} + I_{n0} \sqrt{1 + i\omega\tau_{n0}} \right] \quad (3)$$

where the thermal voltage $V_t = kT/q$, i denotes the imaginary unit, τ_{p0} and τ_{n0} are the minority charge carrier lifetimes, and ω is the radian frequency of the small signal. It is worth noting that the real and imaginary terms in Eq. (3) can be separated using the following equation:

$$\sqrt{1 + i\omega\tau_0} = \pm \left[\sqrt{\frac{\sqrt{1 + \omega^2\tau_0^2} + 1}{2}} + i \sqrt{\frac{\sqrt{1 + \omega^2\tau_0^2} - 1}{2}} \right] \quad (4)$$

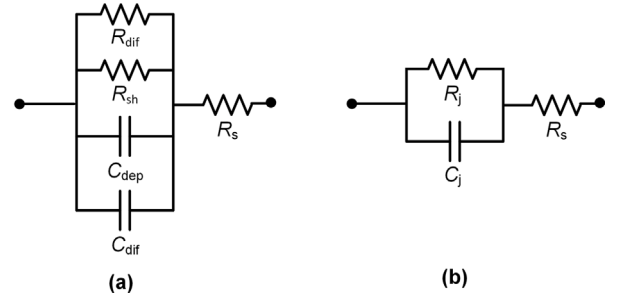


Fig. 1. PN junction equivalent circuits: (a) full circuit, (b) simplified circuit used for the analysis in this work.

No linear, lumped, finite, passive, bilateral network exists that can be synthesized to give the admittance function of Eq. (3) [12]. However, assuming that the frequency is low enough that the minority carrier distribution in the quasi-neutral regions of the junction can follow the AC voltage ($\omega\tau_0 \ll 1$), the approximation $\sqrt{1 + i\omega\tau_0} \approx 1 + i\omega\tau_0/2$ can be made. Substituting this into Eq. (3) yields the following expression for the low-frequency admittance:

$$Y = \frac{1}{V_t} \left[I_{p0} \left(1 + \frac{i\omega\tau_{p0}}{2} \right) + I_{n0} \left(1 + \frac{i\omega\tau_{n0}}{2} \right) \right] \quad (5)$$

As opposed to the admittance in Eq. (3), the low-frequency admittance in Eq. (5) can be described by a lumped passive circuit. Indeed, Eq. (5) can be written in the form:

$$Y = g_{dif} + i\omega C_{dif} \quad (6)$$

with the diffusion conductance g_{dif} and diffusion capacitance C_{dif} both being frequency-independent. However, Eqs. (3) and (4) dictate that as a certain frequency threshold is exceeded, both the real and imaginary part of the admittance are expected to increase with frequency. In the high-frequency limit, the admittance of Eq. (3) simplifies to semi-infinite Warburg admittance [1]. Here, the admittance magnitude increases proportionally to $\sqrt{\omega}$, with equal real and imaginary parts. Physically, Warburg admittance behavior arises whenever a reaction is under partial or complete mass-transport control by diffusion [20].

2.2. Small-signal model

Building on the theory from the previous section, this part introduces the small-signal equivalent circuit of a PN junction. From Eq. (6), it can be deduced that the circuit should include a diffusion resistance R_{dif} and a diffusion capacitance C_{dif} in parallel, to account for the dynamics involved in the diffusion of minority carriers [12]. Additionally, to create a more comprehensive small-signal equivalent circuit of a PN junction, other elements are incorporated. These are a shunt resistance R_{sh} (whose ideal value is very high) and a series resistance R_s . Furthermore, a depletion layer capacitance C_{dep} is introduced to account for the capacitance related to the ionized atoms in the depletion region [12]. The complete small-signal equivalent circuit incorporating all these components is presented in Fig. 1(a). For further analysis, this model is simplified to the one in Fig. 1(b), in which R_j is the parallel of R_{dif} and R_{sh} , and C_j is the parallel of C_{dep} and C_{dif} .

The impedance of the circuit in Fig. 1(b) is given by the following equation:

$$Z = R_s + \left[R_j \parallel \frac{1}{i\omega C_j} \right] \quad (7)$$

Eq. (7) can be rewritten into the form $Z = Z' + iZ''$ with the real part Z' and the imaginary part Z'' being defined as follows:

$$Z' = R_s + \frac{R_j}{1 + R_j^2 \omega^2 C_j^2} \quad (8)$$

$$Z'' = -\frac{R_j^2 \omega C_j}{1 + R_j^2 \omega^2 C_j^2} \quad (9)$$

In Eq. (9), the negative sign can be attributed to the behavior of current and voltage in capacitors. Specifically, in a capacitor, the current leads the voltage, resulting in a negative sign. The impedance of Eq. (7) would ideally produce a semicircle in a Nyquist plot. However, as discussed in Section 2.1, R_{dif} and C_{dif} can be expected to maintain their constant values only below a certain threshold frequency. At frequencies well beyond this threshold, the impedance associated with the diffusion process may begin to resemble a Warburg element, resulting in a -45° feature in the high-frequency part of the Nyquist plot [21–23].

Now that the equivalent circuit and its impedance equations have been established, it is important to highlight distinctions in how the different circuit elements vary with voltage and frequency. In this discussion, the voltage dependence is always derived for PN junctions with homogeneously doped regions. While these conditions are not typically valid in practical devices, they provide a useful starting point for understanding the behavior of these junctions. First, the depletion layer capacitance (C_{dep}) typically dominates C_j at reverse bias and at low forward bias voltage. For a PN junction consisting of homogeneously doped regions, C_{dep} is given by [12]:

$$C_{\text{dep}} = A \sqrt{\frac{q \epsilon_s N_a N_d}{2 (V_{bi} + V_R) (N_a + N_d)}} \quad (10)$$

where ϵ_s is the permittivity of the semiconductor, N_a and N_d are the acceptor and donor concentrations, respectively. V_{bi} is the built-in potential, and V_R is the applied reverse-bias voltage. According to previous publications, it can be assumed that C_{dep} does not relax with frequency [21,24]. Regarding the diffusion resistance R_{dif} and the diffusion capacitance C_{dif} , their values are expected to remain constant as long as the condition $\omega \tau_0 \ll 1$ is satisfied. However, once a threshold frequency is exceeded, Eq. (3) predicts that both R_{dif} and C_{dif} begin to relax with frequency. It is important to note that this threshold frequency depends on the specific device, as τ_0 is determined by the recombination of minority carriers within the device. At low frequencies, the C_{dif} typically dominates C_j at high forward bias voltage. For a PN junction consisting of homogeneously doped regions, C_{dif} is given by [12]:

$$C_{\text{dif}} = \frac{q^2 n_i^2 A}{2kT} \left(\frac{\sqrt{D_p \tau_{p0}}}{N_d} + \frac{\sqrt{D_n \tau_{n0}}}{N_a} \right) \exp \left(\frac{qV_F}{kT} \right) \quad (11)$$

where n_i is the intrinsic carrier concentration and V_F is the applied forward-bias voltage.

3. Simulation approach

In Section 3.1 the model used to generate impedance data is introduced. Subsequently, in Section 3.2 it is explained how these impedance data are analyzed.

3.1. TCAD sentaurus model

In this study, electrical simulations of the semiconductor devices are performed using the finite element simulator TCAD Sentaurus [25]. The two-dimensional device structures simulated in this work are illustrated in Fig. 2. The structure depicted in Fig. 2(a) consists of an n-type bulk and two ideal contacts with no resistance situated at the opposite side of the bulk. The top contact is from now on referred to as the positive contact, with the bottom contact being the negative contact. In this study different variations were investigated, but the results presented are primarily for a contact width of $W_c = 50 \mu\text{m}$, a bulk width of $W_{\text{bulk}} = 500 \mu\text{m}$, a thickness of $t_{\text{bulk}} = 200 \mu\text{m}$, and a substrate/bulk n-type dopant concentration of $N_{\text{sub}} = 1 \times 10^{15} \text{ cm}^{-3}$. The PN structure in

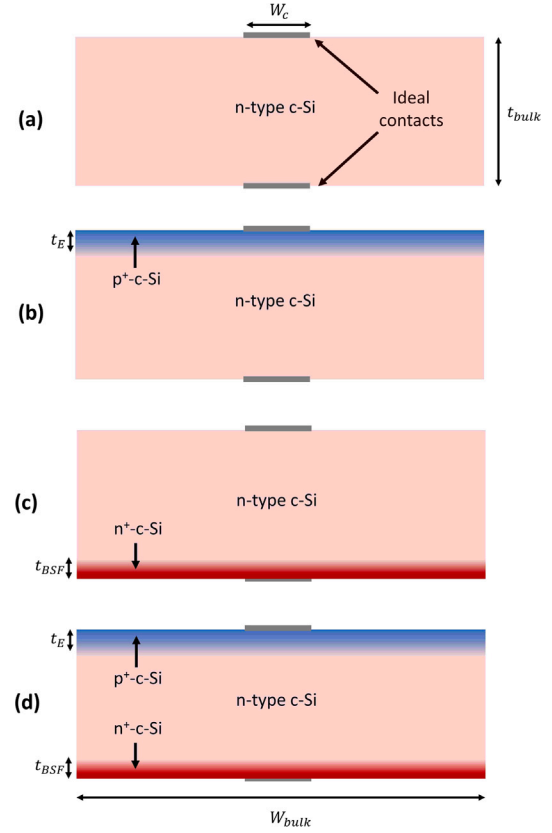


Fig. 2. Simulated structures. Structure (a) consists of only an n-type bulk with two ideal contacts. Unless otherwise specified, in this study the bulk has a thickness t_{bulk} of $200 \mu\text{m}$, a width W_{bulk} of $500 \mu\text{m}$, and a bulk n-type dopant concentration N_{sub} of $1 \times 10^{15} \text{ cm}^{-3}$. The ideal contacts have a width W_c of $50 \mu\text{m}$. Structure (b) includes a p⁺ doped layer near the positive contact, called the emitter. Structure (c) includes an n⁺ doped layer near the negative contact, forming a so-called LH junction or BSF. Both the emitter and the BSF are composed of highly doped p⁺ and n⁺ regions, respectively, with Gaussian doping profiles. Each profile has a peak concentration of $1 \times 10^{19} \text{ cm}^{-3}$ at the surface, and drops to 10% of the peak value at half of their respective junction depths t_E and t_{BSF} , both set at $10 \mu\text{m}$. Finally, structure (d) includes both a PN and LH junction.

Fig. 2(b) is obtained from the former by including a p⁺-doped emitter directly underneath the positive contact. Alternatively, the LH structure in Fig. 2(c) includes an n⁺-doped layer above the negative contact. The interface between this doped region and the bulk is also referred to as the low-high (LH) junction or the back surface field (BSF). It is worth noting that both the p⁺-layer from Fig. 2(b) and the n⁺-layer from Fig. 2(c) have Gaussian doping profiles with a peak concentration of $1 \times 10^{19} \text{ cm}^{-3}$ at the surface, which drops to 10% of the peak value at half of their respective junction depths t_E and t_{BSF} , both set at $10 \mu\text{m}$. Finally, the PN/LH structure in Fig. 2(d) includes both an emitter and LH junction. Since it is expected from Eq. (3) that the minority carrier lifetime plays an important role in the admittance, the trap density in the bulk is an important parameter that can impact both C_j and R_j . In this study, the bulk trap density of the different structures in Fig. 2 is adjusted using a parameter called the Shockley–Read–Hall (SRH) lifetime τ_{SRH} .

The small-signal AC analysis is conducted using the *ACCoupled* solve section of TCAD Sentaurus, assuming dark conditions and a temperature of 25°C . This simulation generates a frequency-dependent impedance matrix, comprising the real and imaginary parts of the impedance at each frequency examined during the AC analysis. In this study, the frequency range of interest spans from $10 \mu\text{Hz}$ to 1 GHz . It is worth noting that in experimental devices, the inductance of the metal contacts dominates the reactance at high frequencies [15], whereas

there is no such inductance in the simulation approach utilized here. Additionally, the use of ideal contacts in the simulation excludes any high-frequency effects that may alter the impedance of metal contacts. Moreover, the simulation data is characterized by low noise levels. Consequently, the simulation data enables the identification of subtle trends strictly related to the impedance of the junctions themselves, which may be more challenging to extract from experimental data.

3.2. Equivalent circuit analysis

The next step involves interpreting the impedance data using the electrical circuit depicted in Fig. 1(b). To extract the values of the different circuit elements, two different methods are employed:

1. CNLS fitting: Complex nonlinear least-squares (CNLS) analysis is utilized to simultaneously fit Eqs. (8) and (9) to the impedance data. This approach, widely applied in the analysis of c-Si solar cells, assumes fixed element values for R_j , C_j , and R_s . However, as explained in Section 2.1, this assumption holds true only up to a certain frequency limit. This study further elaborates on the frequency limitations of this fixed circuit element assumption.
2. Analytic approach: In the simulated device structures, R_s is primarily influenced by the series resistance of the semiconductor bulk. It is generally assumed that R_s is mostly independent of frequency [2], and later in this work it is shown that this is also a valid approximation for the simulated device structures. Moreover, at high frequencies nearing 1 GHz, the real part of the impedance is primarily governed by R_s . Thus, one possible strategy is to extract the R_s value directly from the high-frequency real part of the impedance. If the value of R_s is known, R_j and C_j remain as the two unknowns in Eqs. (8) and (9). Their values can then be analytically computed from the impedance data at each individual frequency value. As such, this method facilitates the analysis of how R_j and C_j vary with frequency. It is worth noting that this analytic approach cannot be used for more complex equivalent circuits with more than two unknowns.

As further elaborated in Section 4, throughout this study the low-frequency values of R_j and C_j from these two different methods closely align. However, differences between the methods emerge as the frequency exceeds a certain threshold.

4. Results

In Section 4.1 the validity of the CNLS and analytic approach are compared over the whole tested frequency range. Subsequently, in Section 4.2 it is demonstrated how the silicon bulk properties influence these results. Finally, Section 4.3 discusses how the impedance changes when a LH junction is added to the device structure. These three sections represent the main findings from this work. Design factors that have a more subtle influence on the impedance, such as variations in the dopant concentration and/or junction depth (t_E and t_{BSF}) of the emitter and BSF, are not reported in this study.

4.1. PN junction impedance at high frequency

In this section, the evolution of the PN junction impedance is discussed as the frequency reaches a level where the minority carrier concentration profile can no longer follow the AC signal. Previous literature suggests that the diffusion capacitance “contributes a frequency-dependent diffusion capacitance to the total capacitance” [26]. Additionally, it has been observed that the diffusion capacitance “relaxes” at high frequencies, meaning that its value reduces with frequency [24]. While discussions often focus on the frequency-dependent behavior of C_j , the frequency-dependence of R_j is typically not discussed, potentially leading readers to assume that R_j remains frequency-independent while C_j decreases with frequency. In some works where a CPE is

used in the equivalent model to address the capacitance variations, the resistive elements are typically fixed [18,19]. However, it is worth pointing out that from Eqs. (3) and (4) it can be deduced that once the frequency exceeds a threshold where the condition $\omega\tau_0 \ll 1$ no longer holds, both the real and imaginary parts of the admittance become frequency-dependent. Specifically, both the real and imaginary parts of the admittance start to increase with frequency, indicating a relaxation of both R_j and C_j . This theoretical prediction aligns with the TCAD simulation results from this study. Figs. 3(a) and 3(b) depict the impedance data of the PN junction structure from Fig. 2(b) at 0 mV and 500 mV DC bias voltage, respectively. Moreover, these plots include the best CNLS and analytic fits. As expected, the fits from the analytic approach perfectly overlap with the data, since a point-by-point fitting is performed. Additionally, in the bottom two plots in Figs. 3(a) and 3(b), the C_j and R_j values extracted from both the CNLS and analytic methods are plotted as a function of frequency.

Fig. 3(a) at 0 mV bias shows that the CNLS method offers a high-quality fit across the entire frequency range. Consequently, it might appear reasonable to conclude that R_j and C_j maintain fixed values throughout the frequency spectrum. Indeed, within the low-frequency range, the analytic approach yields identical values for R_j and C_j as the CNLS approach. However, at higher frequencies, the analytic approach indicates that R_j and C_j begin to relax within the tested frequency range. Here, f_C and f_R denote the frequencies where C_j and R_j , respectively, have dropped below 90% of their low-frequency value. In Fig. 3(a), f_C and f_R are 444 MHz and 1.4 kHz, respectively. While the high value of f_C can be attributed to the dominance of the depletion capacitance, the relatively low value of f_R may seem unexpected, considering the high-quality CNLS fit. However, closer inspection reveals slight deviations between the CNLS fit and the impedance data, although these deviations are relatively minor and may not conclusively demonstrate that R_j has indeed become variable.

Nevertheless, Fig. 3(b) at 500 mV forward bias provides deeper insights. Here, the deviations between the best CNLS fit and the impedance data clearly highlight the shortcomings of fixed circuit elements in accurately describing PN junction physics. The analytic approach suggests that f_R remains similar to the 0 mV bias case, at 3.1 kHz. Moreover, at 500 mV bias, the anticipated variability of C_j becomes noticeable from $f_C = 8.1$ kHz and higher. The lower value of f_C at 500 mV compared to 0 mV can be attributed to the dominance of the diffusion capacitance over C_j in this case. In this study it was confirmed that no good fit can be achieved over the whole frequency range when R_j is held fixed and C_j is calculated at each individual frequency. Instead, the only plausible explanation is that both R_j and C_j relax with increasing frequency when f_R and f_C are exceeded, respectively. Finally, it is worth noting that in Fig. 3(b), the low-frequency value of C_j differs slightly between the CNLS and the analytic method. This difference arises because the CNLS fit is performed over the entire frequency range, also optimizing the fit beyond the frequency where C_j and R_j start to relax.

4.2. Bulk properties influence on PN junction impedance

In PN junctions where one side has a much higher dopant concentration than the other, the impedance is mainly affected by the properties of the lowly doped side of the junction. In the context of solar cells, it is thus important to mention that the substrate dopant concentration has a strong impact on the impedance [15]. However, since this effect is already well-known, the focus in this section shifts toward another bulk property, which is the bulk trap density. Specifically, the influence of bulk trap density is investigated by varying τ_{SRH} in the PN junction structure depicted in Fig. 2(b). Fig. 4(a) illustrates how the low-frequency C_j (determined using the analytic approach) varies as a function of τ_{SRH} for various applied DC bias voltages. At low bias voltage between 0 mV and 200 mV, where the depletion capacitance dominates, C_j does not depend on τ_{SRH} . This observation aligns with

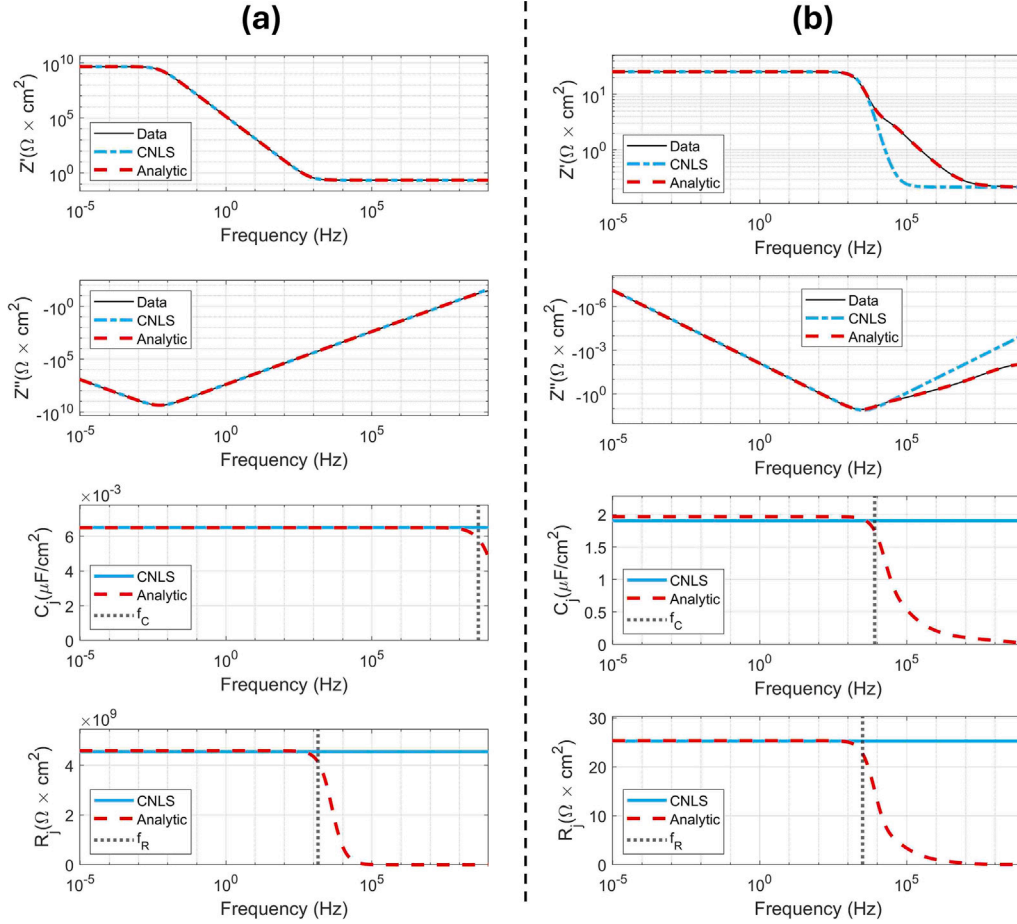


Fig. 3. (a) Impedance analysis of the PN structure shown in Fig. 2(b) at 0 mV bias voltage and $\tau_{\text{SRH}} = 10$ ms. From top to bottom, the real part of the impedance, the imaginary part of the impedance, C_j and R_j are shown as functions of frequency. In the bottom two plots, $f_C = 444$ MHz and $f_R = 1.4$ kHz represent the frequencies where C_j and R_j , respectively, drop below 90% of their low-frequency value. (b) Impedance analysis of the same PN structure under a forward bias voltage of 500 mV, with $\tau_{\text{SRH}} = 10$ ms. The plots follow the same order as in (a), with $f_C = 8.1$ kHz and $f_R = 3.1$ kHz.

Eq. (10), which states that C_{dep} is independent of the minority carrier lifetime. However, at higher bias voltages, a different trend emerges. Specifically, in the range where τ_{SRH} is lower than 10^{-4} s, C_j exhibits a strong increase with τ_{SRH} . It is worth noting that the simulated C_j - τ_{SRH} relationship deviates from the square root dependency predicted by Eq. (11). This deviation arises because, in the simulated device structure with a bulk thickness of 200 μm , a small fraction of carriers recombines at the ideal contacts rather than in the bulk. A reference simulation with a bulk thickness of 1000 μm and a τ_{SRH} variation between 10^{-7} s and 10^{-4} s (not shown in this paper) confirms this, as it exhibits the square root dependency predicted by Eq. (11). Moreover, above $\tau_{\text{SRH}} = 10^{-4}$ s, the dependency of C_j on τ_{SRH} diminishes. Presumably, this trend is attributed to the decreasing dominance of SRH recombination. As the hole diffusion length approaches or exceeds the bulk thickness, the effective lifetime in the bulk becomes dominated by minority carrier recombination at the ideal contacts. Indeed, as the effective hole lifetime increases from 10^{-5} s to 10^{-4} s, the theoretical relationship for the diffusion length ($L_p = \sqrt{D_p \tau_{p0}}$) predicts that L_p increases from 110 μm to 349 μm , hereby exceeding the bulk thickness. In cases where the bulk thickness is much smaller than the minority carrier diffusion length, commonly observed in solar cells, the diode is referred to as a *short diode*. The short diode explanation was further supported by confirming that for low τ_{SRH} , C_j does not depend on the bulk thickness, whereas for high τ_{SRH} , C_j does vary with the bulk thickness. However, these additional results are not included in this article. Furthermore, Fig. 4(b) demonstrates the variation of R_j with

τ_{SRH} . As expected, an increase in τ_{SRH} corresponds to higher R_j values since the spatial distribution of minority carrier holes in the n-type bulk becomes less steep. Similar to the behavior observed for C_j in Fig. 4(a), stabilization occurs as τ_{SRH} approaches levels where the short diode approximation applies. It is worth noting that this stabilization is not observed around 0 mV bias, presumably due to the dominance of generation and recombination currents at low voltages, unlike the diffusion current observed in forward bias [12].

In Fig. 4(c), f_C is plotted as functions of τ_{SRH} . In the low-voltage region, where C_{dep} dominates, f_C remains relatively high and independent of τ_{SRH} . However, in forward bias it can be observed that f_C decreases with increasing τ_{SRH} , with a stabilization occurring towards high τ_{SRH} . Similarly, Fig. 4(d) demonstrates that f_R varies with τ_{SRH} , exhibiting a stabilization trend towards high τ_{SRH} . This stabilization aligns with the earlier explanation that the impedance becomes less influenced by the bulk trap density as τ_{SRH} reaches a value where the short diode approximation becomes valid.

In Fig. 5, the Nyquist spectra of the PN junction devices at 500 mV forward bias are presented for varying τ_{SRH} values ranging from 10^{-7} s to 10^{-2} s. In each plot, f_R and f_C are highlighted. Notably, f_R and f_C decrease as τ_{SRH} becomes higher. However, since the values of R_j and C_j change as well, f_R and f_C consistently fall within the frequency regime where the Nyquist spectra are near the top of the semi-circle. Consequently, all plots visibly deviate from the semi-circular shape expected of an RC-loop, indicating the frequency-dependence of R_j and C_j . However, it must be noted that the shape of the Nyquist spectra may

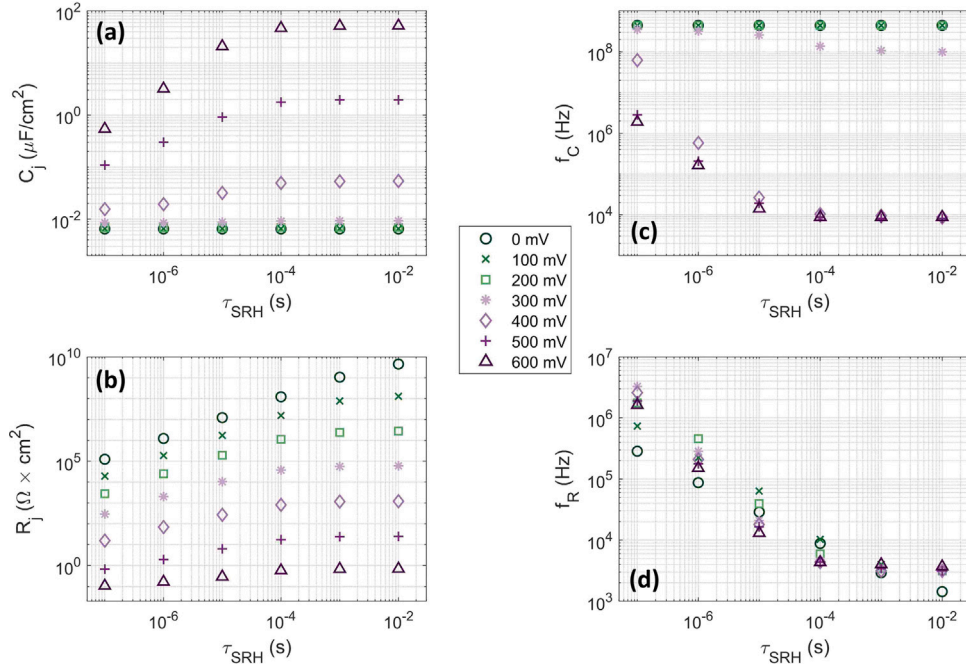


Fig. 4. Equivalent circuit element analysis of the PN structure of Fig. 2(b). In (a) and (b), the low-frequency C_j and R_j , which are determined using the analytic method, are presented as a function of τ_{SRH} for various DC bias voltages, respectively. Moreover, in (c) and (d), f_C and f_R are plotted as functions of τ_{SRH} for various DC bias voltages. f_C and f_R denote the frequencies where C_j and R_j , respectively, have dropped below 90% of their low-frequency value.

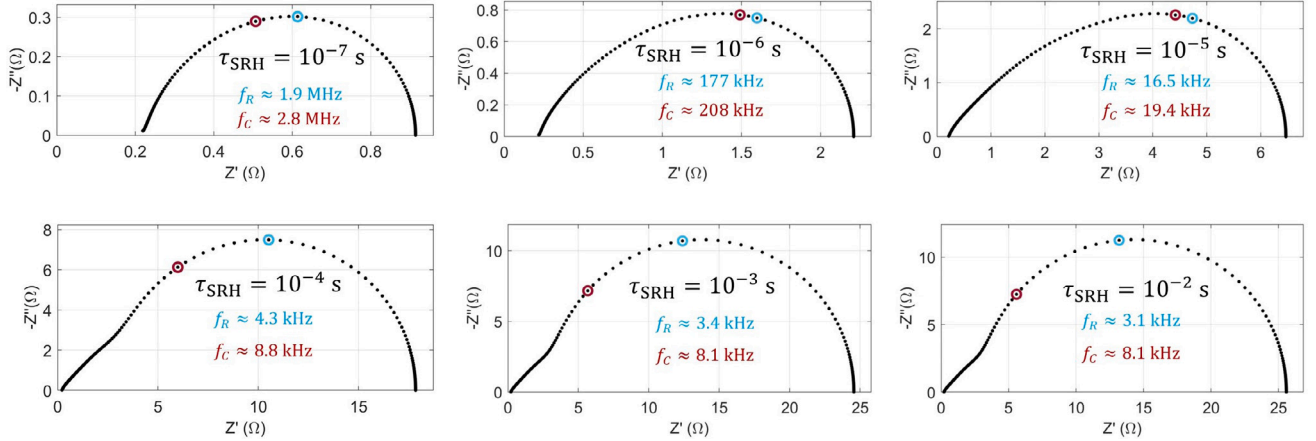


Fig. 5. Nyquist spectra of the PN structure of Fig. 2(b) at 500 mV forward bias for varying τ_{SRH} . f_C and f_R are highlighted in each plot.

change when a LH junction is added at the negative contact. Further discussion on this topic is provided in the next section.

4.3. Low-high junction influence

In this section, the influence of a highly doped n^+ -layer on the impedance is examined. As previously mentioned, practical c-Si solar cells commonly incorporate such a LH junction, also known as a back surface field (BSF). In addition to facilitating tunneling, the BSF serves as a barrier that prevents minority holes in the n-region from diffusing to the defective metal-semiconductor interface [27]. Consequently, SRH recombination is reduced and the open-circuit voltage (V_{oc}) is enhanced. In literature on impedance spectroscopy for c-Si solar cells, the LH junction is often accounted for by incorporating an additional RC-loop into the equivalent circuit of the device [2,4,14–17]. However, there is limited discussion on comparing the impedance of PN junction devices with and without a BSF. Presumably, this is because

practical devices inherently contain such a junction, making it challenging to experimentally test a device without it. With the simulation approach utilized in this study, further insights can be obtained about the impedance of the LH junction. Comparing an n-type bulk structure (Fig. 2(a)) with a similar structure incorporating a LH junction at the negative contact (Fig. 2(c)), the impedance spectra are plotted in Fig. 6.

In Fig. 6 it is evident that the Z' of the LH structure is slightly lower than that of the bulk structure, which is due to the higher conductivity in the n^+ layer. Moreover, it can be observed from Fig. 6 that both impedance spectra exhibit predominantly resistive behavior, with Z' remaining constant and Z'' negligibly small across most frequencies. Hence, it is worth noting that this result confirms the validity of assuming a constant R_s value in the analytic approach employed in this study. Only at the upper-frequency limit does Z'' become measurably large compared to Z' , leading to a -1.7° phase shift at 1 GHz. The evolution of Z'' with frequency in Fig. 6 appears in both the bulk structure with and without the LH junction. This effect is presumably due to the device's geometric capacitance, with the silicon bulk acting

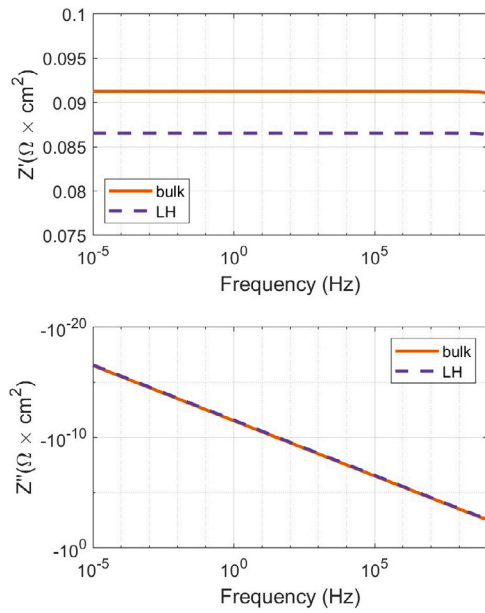


Fig. 6. Impedance of the n-type bulk structure of Fig. 2(a) and the n-type bulk with n^+ -doped LH structure of Fig. 2(c). $\tau_{SRH} = 10$ ms and W_c and W_{bulk} are both equal to 500 μm . The plots are for 0 mV bias, but the results are nearly identical when a positive bias voltage is applied to the bulk contact with respect to the BSF contact.

as the dielectric and the contacts as plates. However, in real-world devices this effect would likely be obscured, as inductance tends to dominate Z'' at high frequencies. Consequently, two key observations emerge from Fig. 6. Firstly, the LH junction device structure exhibits lower Z' compared to the bulk, meaning that the LH junction only lowers the series resistance and does not introduce additional resistive effects. Secondly, the LH junction itself does not seem to introduce dynamic effects within the frequency range of interest.

In spite of the previous observations, the presence of a LH junction can significantly affect the impedance of a full PN junction device. To illustrate this, the impedance of (1) a PN device structure and (2) a PN/LH device structure are depicted in Fig. 7. In the simulations it was observed that for both bias voltages, the electrostatic potential across the PN junction remains virtually unchanged between the device structures with and without the LH junction. This is related to the fact that the applied voltage mainly drops across the PN junction, rather than over the LH junction. Therefore, the differences in the impedance spectra due to addition of a LH junction are not related to changes in the bias voltage across the PN junction.

In the case of the 0 mV bias voltage depicted in Fig. 7(a–b), there is a noticeable difference in the overall impedance between the two structures. Using the analytic approach, the differences in R_s and the low-frequency values of R_j and C_j upon addition of the LH junction are compared. The low-frequency R_j increases from $4.54 \times 10^9 \Omega\text{cm}^2$ to $1.25 \times 10^{10} \Omega\text{cm}^2$, while R_s decreases from $0.22 \Omega\text{cm}^2$ to $0.088 \Omega\text{cm}^2$. The increase in R_j can primarily be attributed to the fact that the BSF repels minority carriers from the negative contact. Consequently, the distribution of minority carriers throughout the bulk becomes less steep, resulting in an increase in R_j . Conversely, the decreased R_s can be attributed to the enhanced lateral charge carrier transport within the highly doped region of the LH junction. It is worth noting that the low-frequency C_j remains unchanged at 6.50 nF/cm^2 between the two device structures. This consistency can be attributed to the fact that the depletion capacitance solely relies on the ionized atoms within the depletion region of the PN junction.

For the 500 mV case in Fig. 7(c–d), the addition of the LH junction increases the low-frequency R_j from $25.3 \Omega\text{cm}^2$ to $801 \Omega\text{cm}^2$. R_s is again decreased from $0.22 \Omega\text{cm}^2$ to $0.088 \Omega\text{cm}^2$. The explanations are

similar to the 0 mV case. However, opposed to the 0 mV case, the addition of the LH junction at 500 mV increases the low-frequency C_j from $1.97 \mu\text{F/cm}^2$ to $2.72 \mu\text{F/cm}^2$. This increase can be attributed to the fact that the BSF repels the minority carrier holes from the negative contact, increasing the effective lifetime of holes stored in the silicon bulk. Furthermore, it is worth reflecting how the addition of the LH junction affects the Nyquist plots. The Nyquist spectra at 500 mV bias are presented in Fig. 7(e) for the PN device, and in Fig. 7(f) for the PN/LH device. At first glance, the Nyquist spectrum of the device with the PN/LH junction seems to closely resemble a semi-circular shape, as opposed to the PN structure. However, the zoomed-in view in Fig. 7(f) shows that the high-frequency variations of R_j and C_j still occur and create distortions to the high-frequency tail of the Nyquist spectrum.

In this section, it was demonstrated that the LH junction exhibits no significant impedance characteristics by itself. This finding contrasts with existing literature, where the LH junction is often represented as an additional RC-loop in series with the R_j - C_j loop [2,4,14–17]. Indeed, particular combinations of parameters in devices with a PN/LH structure can result in a Nyquist plot resembling that of two RC-loops in series. For instance, Fig. 8 illustrates how the Nyquist spectra of a PN/LH device changes when the bulk dopant concentration is changed between $N_{sub} = 1 \times 10^{15}$ and $N_{sub} = 5 \times 10^{16} \text{ cm}^{-3}$. While one resembles a single semicircle, the other might be mistaken for two superimposed semicircles. However, this study suggests that the inclusion of an R_{LH} - C_{LH} loop to the model does not accurately represent the underlying physics. Instead, its inclusion in the model appears to account for the frequency-dependent variations in R_j and C_j . Throughout our investigation, instances were observed where the two RC-loop model falls short in explaining the impedance spectra adequately, indicating that the relaxation of R_j and C_j is a more plausible explanation. Moreover, such relaxation phenomena cannot always be easily detected through Nyquist plots on linear scales. Therefore, Bode plots or real and imaginary impedance plots on a logarithmic scale often provide better insights.

5. Conclusion

The impedance characteristics of PN homojunction devices were investigated, particularly focusing on the effects of frequency, applied bias voltage, bulk trap density, and the presence of a low-high (LH) junction or back surface field (BSF). The employed TCAD simulation method allows to detect subtle trends that may be difficult to identify experimentally due to noise and reactance of metal contacts. Through analysis of the impedance data it was shown that the PN junction exhibits a fixed RC-loop behavior at low frequencies, but undergoes relaxation in both resistance R_j and capacitance C_j as frequency increases. Additionally, it was found that when the bulk defect density decreases below a certain threshold, the effective minority carrier lifetime in the bulk becomes limited by recombination at the contacts. In this regime, the short diode approximation effectively explains various observed impedance trends and factors such as wafer thickness and the presence of a BSF strongly affect the impedance. Notably, it was shown that the addition of a LH junction repels minority carriers from this contact, hereby impacting the impedance by altering R_j , C_j , and R_s . Contrary to conventional modeling approaches, which often include an additional RC-loop to represent the LH junction, this study suggests that such a representation does not represent the underlying physics, particularly the frequency-dependent behavior of R_j and C_j . These insights are important for solar-cell applications that require a thorough understanding of the small-signal response. Moreover, this work serves as a basis for fully understanding the impedance of solar cells with passivating contacts.

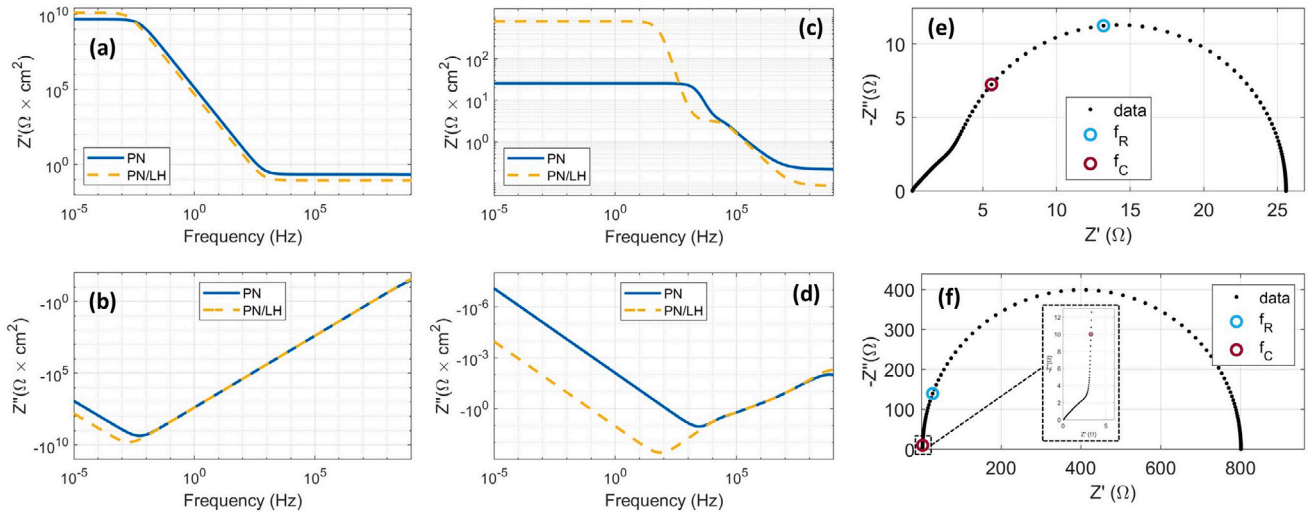


Fig. 7. Comparison between the impedance of the PN structure of Fig. 2(b) and the PN/LH structure of Fig. 2(d) for $\tau_{SRH} = 10$ ms. (a) and (b) present the impedance at 0 mV bias, whereas (c) and (d) are at 500 mV forward bias. Finally, (e) and (f) show the Nyquist spectra at 500 mV forward bias of the PN and PN/LH structure, respectively. For the PN structure at 500 mV bias, f_R and f_C are 3.1 kHz and 8.1 kHz, respectively. In contrast, for the PN/LH structure, f_R and f_C decrease to 0.40 kHz and 5.9 kHz, respectively.

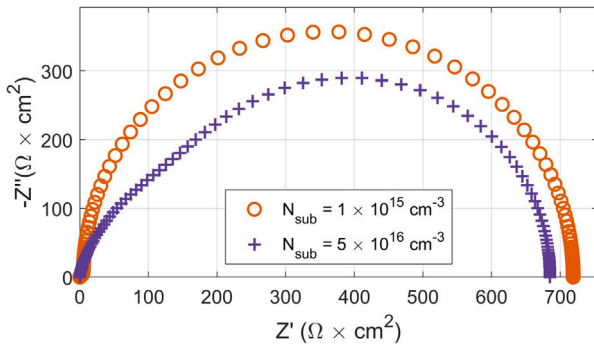


Fig. 8. Nyquist spectra of the PN/LH structure of Fig. 2(d) for wafer dopant concentration values of $N_{sub} = 1 \times 10^{15} \text{ cm}^{-3}$ and $N_{sub} = 5 \times 10^{16} \text{ cm}^{-3}$. The impedance data are recorded at 500 mV forward bias with the bulk properties set at $\tau_{SRH} = 10$ ms and $t_{bulk} = 300 \text{ } \mu\text{m}$.

CRediT authorship contribution statement

David A. van Nijen: Writing – review & editing, Writing – original draft, Visualization, Validation, Software, Project administration, Methodology, Investigation, Formal analysis, Data curation, Conceptualization. **Paul Procel:** Methodology. **René A.C.M.M. van Swaaij:** Writing – review & editing. **Miro Zeman:** Funding acquisition. **Olindo Isabella:** Writing – review & editing, Supervision, Funding acquisition. **Patrizio Manganiello:** Writing – review & editing, Supervision, Software, Project administration, Methodology, Formal analysis, Conceptualization.

Declaration of Generative AI and AI-assisted technologies in the writing process

During the preparation of this work the author(s) used ChatGPT in order to improve the text flow. After using this tool/service, the author(s) reviewed and edited the content as needed and take(s) full responsibility for the content of the published article.

Declaration of competing interest

The authors declare that they have no known competing financial interests or personal relationships that could have appeared to influence the work reported in this paper.

Acknowledgments

This work is supported by the sector plan of the Dutch government in photovoltaics research, The Netherlands.

Data availability

The dataset underlying this article is available in the 4TU Research Database, accessible via this link: <https://doi.org/10.4121/19445ed8-c8d5-4204-a8c6-adaa7a55ece3>.

References

- [1] I. Mora-Seró, G. Garcia-Belmonte, P.P. Boix, M.A. Vázquez, J. Bisquert, Impedance spectroscopy characterisation of highly efficient silicon solar cells under different light illumination intensities, *Energy Environ. Sci.* 2 (2009) 678–686, <http://dx.doi.org/10.1039/B812468J>.
- [2] J.E. Garland, D.J. Crain, J.P. Zheng, C.M. Sulyma, D. Roy, Electro-analytical characterization of photovoltaic cells by combining voltammetry and impedance spectroscopy: voltage dependent parameters of a silicon solar cell under controlled illumination and temperature, *Energy Environ. Sci.* 4 (2011) 485–498, <http://dx.doi.org/10.1039/C0EE00307G>.
- [3] I. Mora-Seró, Y. Luo, G. Garcia-Belmonte, J. Bisquert, D. Muñoz, C. Voz, J. Puigdollers, R. Alcubilla, Recombination rates in heterojunction silicon solar cells analyzed by impedance spectroscopy at forward bias and under illumination, *Sol. Energy Mater. Sol. Cells* 92 (4) (2008) 505–509, <http://dx.doi.org/10.1016/j.solmat.2007.11.005>.
- [4] J. Panigrahi, Vandana, R. Singh, N. Batra, J. Gope, M. Sharma, P. Pathi, S. Srivastava, C. Rauthan, P. Singh, Impedance spectroscopy of crystalline silicon solar cell: Observation of negative capacitance, *Sol. Energy* 136 (2016) 412–420, <http://dx.doi.org/10.1016/j.solener.2016.06.041>.
- [5] D.A. van Nijen, P. Manganiello, M. Zeman, O. Isabella, Exploring the benefits, challenges, and feasibility of integrating power electronics into c-Si solar cells, *Cell Rep. Phys. Sci.* 3 (7) (2022) 100944, <http://dx.doi.org/10.1016/j.xcrp.2022.100944>.
- [6] J.-H. Huang, B. Lehman, T. Qian, Submodule integrated boost DC-DC converters with no external input capacitor or input inductor for low power photovoltaic applications, in: 2016 IEEE Energy Conversion Congress and Exposition, ECCE, 2016, pp. 1–7, <http://dx.doi.org/10.1109/ECCE.2016.7855476>.
- [7] H. Ziar, P. Manganiello, O. Isabella, M. Zeman, Photovoltaics: intelligent PV-based devices for energy and information applications, *Energy Environ. Sci.* 14 (2021) 106–126, <http://dx.doi.org/10.1039/D0EE02491K>.
- [8] S.-M. Kim, J.-S. Won, S.-H. Nahm, Simultaneous reception of solar power and visible light communication using a solar cell, *Opt. Eng.*, Bellingham 53 (4) (2014) 046103.
- [9] R. Sarwar, B. Sun, M. Kong, T. Ali, C. Yu, B. Cong, J. Xu, Visible light communication using a solar-panel receiver, in: 2017 16th International Conference on Optical Communications and Networks, ICOCN, 2017, pp. 1–3, <http://dx.doi.org/10.1109/ICOCN.2017.8121577>.

- [10] Y. Zhou, A. Ibrahim, M. Muttillio, P. Manganiello, H. Ziar, O. Isabella, Bandwidth characterization of c-Si solar cells as VLC receiver under colored LEDs, in: 2023 8th International Conference on Smart and Sustainable Technologies (SpliTech), 2023, pp. 1–5, <http://dx.doi.org/10.23919/SpliTech58164.2023.10193624>.
- [11] Y. Zhou, A. Ibrahim, M. Muttillio, H. Ziar, O. Isabella, P. Manganiello, Investigation on simultaneous energy harvesting and visible light communication using commercial c-Si PV cells: Bandwidth characterization under colored LEDs, Energy 311 (2024) 133387, <http://dx.doi.org/10.1016/j.energy.2024.133387>.
- [12] D.A. Neamen, Semiconductor Physics and Devices, fourth ed., McGraw Hill Education, 2012.
- [13] T.G. Allen, J. Bullock, X. Yang, A. Javey, S.D. Wolf, Passivating contacts for crystalline silicon solar cells, Nature Energy 4 (11) (2019) 914–928, <http://dx.doi.org/10.1038/s41560-019-0463-6>.
- [14] D.J. Crain, J.E. Garland, S.E. Rock, D. Roy, Quantitative characterization of silicon solar cells in the electro-analytical approach: Combined measurements of temperature and voltage dependent electrical parameters, Anal. Methods 4 (2012) 106–117, <http://dx.doi.org/10.1039/C1AY05455D>.
- [15] D.A. van Nijen, M. Muttillio, R. Van Dyck, J. Poortmans, M. Zeman, O. Isabella, P. Manganiello, Revealing capacitive and inductive effects in modern industrial c-Si photovoltaic cells through impedance spectroscopy, Sol. Energy Mater. Sol. Cells 260 (2023) 112486, <http://dx.doi.org/10.1016/j.solmat.2023.112486>.
- [16] O.I. Olayiwola, P.S. Barendse, Photovoltaic cell/module equivalent electric circuit modeling using impedance spectroscopy, IEEE Trans. Ind. Appl. 56 (2) (2020) 1690–1701, <http://dx.doi.org/10.1109/TIA.2019.2958906>.
- [17] P. Yadav, K. Pandey, V. Bhatt, M. Kumar, J. Kim, Critical aspects of impedance spectroscopy in silicon solar cell characterization: A review, Renew. Sustain. Energy Rev. 76 (2017) 1562–1578, <http://dx.doi.org/10.1016/j.rser.2016.11.205>.
- [18] M.M. Shehata, T.N. Truong, R. Basnet, H.T. Nguyen, D.H. Macdonald, L.E. Black, Impedance spectroscopy characterization of c-Si solar cells with SiO₂/ Poly-Si rear passivating contacts, Sol. Energy Mater. Sol. Cells 251 (2023) 112167, <http://dx.doi.org/10.1016/j.solmat.2022.112167>.
- [19] J. Panigrahi, A. Pandey, S. Bhattacharya, A. Pal, S. Mandal, V. Krishna Komarala, Impedance spectroscopy of amorphous/crystalline silicon heterojunction solar cells under dark and illumination, Sol. Energy 259 (2023) 165–173, <http://dx.doi.org/10.1016/j.solener.2023.05.030>.
- [20] S.R. Taylor, E. Gileadi, Physical Interpretation of the Warburg Impedance, Corrosion 51 (9) (1995) 664–671, <http://dx.doi.org/10.5006/1.3293628>.
- [21] P. Casolaro, V. Izzo, G. Giusi, N. Wyrsh, A. Aloisio, Modeling the diffusion and depletion capacitances of a silicon pn diode in forward bias with impedance spectroscopy, J. Appl. Phys. 136 (11) (2024) 115702, <http://dx.doi.org/10.1063/5.0230008>.
- [22] K. Ariyoshi, Z. Siroma, A. Mineshige, M. Takeno, T. Fukutsuka, T. Abe, S. Uchida, Electrochemical impedance spectroscopy part 1: Fundamentals, Electrochemistry 90 (10) (2022) 102007, <http://dx.doi.org/10.5796/electrochemistry.22-66071>.
- [23] E. von Hauff, Impedance Spectroscopy for Emerging Photovoltaics, J. Phys. Chem. C 123 (18) (2019) 11329–11346, <http://dx.doi.org/10.1021/acs.jpcc.9b00892>.
- [24] M.L. Lucia, J.L. Hernandez-Rojas, C. Leon, I. Mártel, Capacitance measurements of p-n junctions: depletion layer and diffusion capacitance contributions, Eur. J. Phys. 14 (2) (1993) 86, <http://dx.doi.org/10.1088/0143-0807/14/2/009>.
- [25] Synopsis, Sentaurus device user, 2021.
- [26] M. Green, M. Gunn, The capacitance of abrupt p-n junction diodes under forward bias, Phys. Status Solidi a 19 (1) (1973) K93–K96.
- [27] A. Smets, K. Jäger, O. Isabella, R. van Swaaij, M. Zeman, Solar energy - The physics and engineering of photovoltaic conversion technologies and systems, Solar Energy - the Physics and Engineering of Photovoltaic Conversion Technologies and Systems, UIT Cambridge Ltd, 2016.